

# A Coastal Bay Summer Breeze Study, Part 2: High-resolution Numerical Simulation of Sea-breeze Local Influences

Isabelle Calmet<sup>1,2</sup> · Patrice G. Mestayer<sup>2</sup> ·  
Alexander M.J. van Eijk<sup>1,3</sup> · Olivier Herlédant<sup>1</sup>

Received: 7 January 2017 / Accepted: 31 October 2017 / Published online: 5 December 2017  
© Springer Science+Business Media B.V., part of Springer Nature 2017

**Abstract** We complete the analysis of the data obtained during the experimental campaign around the semi circular bay of Quiberon, France, during two weeks in June 2006 (see Part 1). A reanalysis of numerical simulations performed with the Advanced Regional Prediction System model is presented. Three nested computational domains with increasing horizontal resolution down to 100 m, and a vertical resolution of 10 m at the lowest level, are used to reproduce the local-scale variations of the breeze close to the water surface of the bay. The Weather Research and Forecasting mesoscale model is used to assimilate the meteorological data. Comparisons of the simulations with the experimental data obtained at three sites reveal a good agreement of the flow over the bay and around the Quiberon peninsula during the daytime periods of sea-breeze development and weakening. In conditions of offshore synoptic flow, the simulations demonstrate that the semi-circular shape of the bay induces a corresponding circular shape in the offshore zones of stagnant flow preceding the sea-breeze onset, which move further offshore thereafter. The higher-resolution simulations are successful in reproducing the small-scale impacts of the peninsula and local coasts (breeze deviations, wakes, flow divergences), and in demonstrating the complexity of the breeze fields close to the surface over the bay. Our reanalysis also provides guidance for numerical simulation strategies for analyzing the structure and evolution of the near-surface breeze over a semi-circular bay, and for forecasting important flow details for use in upcoming sailing competitions.

---

✉ Patrice G. Mestayer  
patrice.mestayer@orange.fr

Isabelle Calmet  
isabelle.calmet@ec-nantes.fr

<sup>1</sup> Laboratoire de recherche en Hydrodynamique, Énergétique et Environnement Atmosphérique (LHEEA), UMR 6598 CNRS – École Centrale de Nantes, 44321 Nantes Cedex 3, France

<sup>2</sup> Institut de Recherche en Sciences et Techniques de la Ville (IRSTV), FR CNRS 2488, Nantes, France

<sup>3</sup> TNO, The Hague, The Netherlands

**Keywords** Coastal meteorology · Complex coastline · Inshore sailing competition · Large-eddy simulation · Sea breeze

## 1 Introduction

Recent years have seen a proliferation of interest in coastal breezes. These breezes largely influence the local meteorology and climatology, which in turn can impact the touristic appeal of a site and, hence, the local economy. The breeze-flow regime may also affect the dispersion of pollutants generated by growing cities in the highly-populated coastal areas, and thereby the air quality. Finally, the assessment of the wind speed close to the coast and further offshore, the changes in the wind direction during the day, and the relationship with the mesoscale meteorology are of critical importance for the development of offshore wind farms.

In addition, the participants of sailing competitions have a great interest in the direction and speed of the flow in the lowest 10–20 m above the sea surface, as well as the variations during the day and from one place to another over the competition area. Such competitions often take place within a coastal bay, with local-scale inshore and offshore processes and temporal variations largely influencing the race strategy. Numerical simulations are known to be used by some top-level competition teams, but their modelling methodology and results do not appear in the open literature. Specific software tools for offshore-sailing races are commercially available, but state-of-the-art meteorological models are not often used in this context. Assessing the numerical-modelling capabilities for simulating the sea-breeze regimes at real sites is, therefore, of increasing importance for not only engineering and environmental purposes but also for sailing competitions.

Our cooperative project was aimed at bridging this gap by involving specialists in preparation of top-level sailing competitions, in the assessment of the hydrodynamic performance of sailing boats, and in the understanding of the dynamics of the lower atmosphere. We performed a two-week experimental campaign in June 2006 over the bay of Quiberon, which is located in the Brittany region of France (Fig. 1) (Barré et al. 2007). In addition, several two-day periods were simulated by Herlédant (2011) with the Advanced Regional Prediction System (ARPS) model at a high spatial resolution. A presentation of the Quiberon 2006 measurements and an analysis of the experimental results are given in Part 1 (see Mestayer et al. 2018). In Part 2, we focus on numerical simulations with the dual purpose of, (i) complementing the observations for understanding the effect of the bay configuration on the local sea breeze, and (ii) producing a proof-of-principle for the assistance of numerical modelling in the planning of sailing races.

Most numerical studies of sea-breeze systems have dealt with perfect or approximate rectilinear coastlines, and focused on the breeze-front penetration inland, the breeze-flow depth (Miller et al. 2003), and/or the breeze-cell structure (Steele et al. 2013). Crosman and Horel's (2010) review shows that recent studies with high-resolution numerical models have mostly focused on the inland penetration of the sea- and lake-breeze front, on the interactions of the breeze flow with terrain-induced convective structures, similar to recent studies of the Marseille area (Leroyer et al. 2010; Calmet and Mestayer 2016), or on heuristic studies of idealized, rectilinear coasts (Antonelli and Rotunno 2007; Crosman and Horel 2010; Steele et al. 2013). In contrast, we focus here on the maritime domain and the influence of the complexity of the coastline. The simulations permit visualization of the velocity field at the

lowest levels over the sea surface in real situations over the coastal semi-circular bay formed by the narrow Quiberon peninsula perpendicular to the continental coast.

In 2005, the original objective of these numerical simulations was to evaluate state-of-the-art and well-validated meteorological models. This work was part of a national program joining scientists and high-level competitors, with a preliminary experiment in 2006 in preparation for a larger cooperative campaign. Due to funding cuts, this main experiment was cancelled and the exploratory numerical simulations were completed within an academic framework (Herlédant 2011), without the expected sensitivity studies. Herlédant (2011) focused on the applicability of the quadrant theory of the synoptic flow for the onset of sea breezes, as well as the design of the experimental campaign in the wider prospect of characterizing the surface flow. Note that several of the choices in the modelling strategy reanalyzed here must be considered in the context of the model improvements of the previous ten years. Unfortunately, our reanalysis is hampered by a computer problem that deprived us of most modelling results, except the velocity and temperature fields at the model's lowest level close to the surface, preventing us from showing the complex three-dimensional structure of the simulated flows (breeze cell and return flow aloft). Furthermore, Hu et al. (2013) reported a problem in the Weather Research and Forecasting (WRF) model (prior to version 3.4.1) that casts serious doubts on any results obtained during stable stratification, which may have affected our simulations of the flow evolution during nighttime and transitional periods, and thus limits our reanalysis to the daytime simulations. Nevertheless, the results still offer an unprecedented view of the surface-flow patterns, demonstrating diverse influences of the local coast on the flow over the semi-circular bay, and the similarities and differences with the breeze structure at a rectilinear shoreline. Therefore, the available results deserve a reanalysis and publication along with the comprehensive and accompanying experimental data reported in Part 1. However, we limit our reanalysis of Herlédant (2011) simulations to the daytime parts of the two days on 23 and 27 June 2006 analyzed in detail in Part 1, to rule out any impact of the WRF-model problem.

As mentioned above, the Quiberon 2006 measurements are presented in Part 1, including an analysis of the most representative experimental results, and a summary of the main practical theories for offshore sea breezes. These include: (i) the influence of the coastal proximity on local wind-speed variations resulting from both the different sea- and land-surface roughness and the coastline flow convergence/divergence (depending on the wind direction), (ii) the quadrant theory for the influence of the synoptic flow on breeze onset, and (iii) the daytime clockwise (veering) or anti-clockwise (backing) rotation of the breeze direction. These theories were initially developed by Adams (1997), and popularized by Houghton and Campbell (2005), and by Bernot (2007) in France. The quadrant theory is based on the classification of synoptic wind directions into four quadrants with respect to the coastline (see Fig. 2a), and is only summarized very briefly here, since it is described in detail by Miller et al. (2003) and in Part 1.

When the synoptic flow is absent or very weak, a pure sea breeze appears perpendicular to the coastline and grows progressively in strength and distance offshore, with increasing temperature difference between the land and sea surfaces. The offshore synoptic flows from quadrants 1 (Q1) and 2 (Q2) (see Fig. 1 of Part 1, and Fig. 2a below) are favourable to a breeze onset because they support an upper-level return flow. For quadrant-1 flows, the breeze extends offshore progressively from the shoreline, with an anti-clockwise rotation of the wind direction (backing from the synoptic wind direction towards the normal to the coast) generally observed during the onset phase. For quadrant-2 flows, convergence over the shoreline tends to both inhibit the breeze front from penetrating inland and perturb or weaken the circulation in the breeze cell; at the sea surface, the breeze initially appears at

some distance offshore, while separated from the shore by bands of opposing and/or stagnant flow. [Houghton and Campbell \(2005\)](#) consider that a characteristic feature of the breeze onset for quadrant-2 flows is the appearance of two separated bands of stagnant flow parallel to the shoreline, which initialize the propagation of an outer and inner breeze front offshore and inland, respectively.

The synoptic wind directions corresponding to quadrants 3 and 4 (Q3 and Q4) are unfavourable to the establishment of a sea-breeze circulation since the flow at higher altitudes is opposite to the development of the breeze return flow. These situations are termed “synoptic” because the local surface flow has approximately the same direction as the synoptic wind direction. However, since the synoptic-scale pressure gradient is generally angled to the coast ([Adams 1997](#)), the surface pressure appears lower inland than offshore in the case of quadrant 3. Hence, the local pressure decrease induced by the daytime warming of the land then increases the horizontal pressure gradient, and it is this thermal reinforcement that moderately increases the onshore surface flow, and deviates this flow towards the left. The thermal component of the flow increases more within the first few kilometres from the shore than further offshore ([Houghton and Campbell 2005](#)).

During our experimental campaign, the synoptic wind speed and direction were deduced from the surface isobars from the hourly surface maps provided by Météo France (see Part 1). In the offshore synoptic-flow condition on 23 June we observed most of the expected characteristics of the sea breeze, with a full 360° clockwise rotation of the breeze direction during the day, and specific small-scale influences of the Quiberon peninsula. For the oblique onshore synoptic flow in 27 June, we observed the rise of an unexpectedly large “synoptic breeze” with a small rotation towards the offshore direction (see Part 1).

Here, we focus our reanalysis of [Herlédant’s](#) simulations on: (i) the surface wind speed and direction as a function of the average and local shoreline directions during the breeze episodes of 23 and 27 June 2006; (ii) the relationship between the small-scale flow and mesoscale meteorological features; (iii) the assessment of current model capabilities in capturing the small-scale processes, and the local influences of sea-breeze flows at low altitudes over the water body and coastline; (iv) the modelling strategy needed to be adopted to analyze the site of an inshore sailing competition.

The set-up of the numerical simulation is described in the next section, with Sect. 3 presenting a point-to-point comparison of the simulation results with the experimental data obtained at the three measurement sites during the two daytime periods of interest. This comparison allows us to identify the successes and failures of the simulations. The daytime breeze successfully simulated at high resolution is examined in detail in Sect. 4, followed by the re-evaluation in Sect. 5 of [Herlédant \(2011\)](#) modelling approach in light of recent improvements in model performance. Finally, Sect. 6 summarizes our conclusions concerning the observed breeze processes in the bay, including the lessons learned about the simulation strategy, with suggestions for possible improvements in the future.

## 2 Numerical Simulation Set-up

The simulation of local topographic influences on the flow close to the bay surface requires a numerical model with a high spatial resolution. Considering that the relevant topographical structures in the area (river mouths, islands, Penthièvre isthmus, Quiberon relief) have a typical scale of 500 m, the ARPS model ([Xue et al. 2000](#)) was used with a horizontal grid spacing  $\Delta x = 100$  m for resolution of the details of the underlying terrain, as well as turbulent



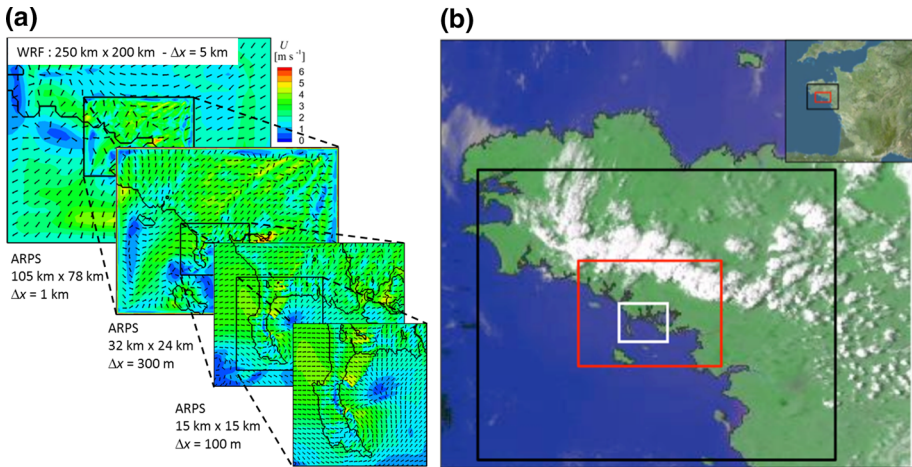


**Fig. 1** Definition of the study area: **a** sketch of the modelling strategy with four nested simulation domains (1300 UTC on 23 June), **b** map of Brittany with the WRF, ARPS-1km and ARPS-300m model-simulation domains (black, red and white rectangles, respectively).

scales of about  $4\Delta x$  (Chow et al. 2006). Close to the surface, a very fine vertical grid spacing of  $\Delta z = 10$  m was employed, together with a vertically-stretched grid above to minimize the number of cells throughout the planetary boundary layer (PBL).

At the same time, the numerical domain must cover several hundreds of kilometres since the thermal coastal breezes are triggered by meteorological conditions at the mesoscale ( $\sim 10^2$  km). The strategy of Herlédant (2011) was based on the one-way off-line grid nesting capability of the ARPS model with the finest (100 m) grid covering the peninsula, the bay and the northern shores, an intermediate grid with a horizontal resolution of 300 m, and a larger domain with a grid resolution of 1 km (see Fig. 1a and Table 1). A resolution ratio close to three was considered optimal for minimizing the number of nested domains while ensuring a good transmission of the flow dynamics. This larger 1-km domain, which is approximately 100 km in size, was still found to be too small to correctly assimilate the meteorological conditions responsible for the breeze at the mesoscale. The WRF mesoscale model operating with a Reynolds-averaged turbulence parametrization at a grid resolution of 5 km was, therefore, used to assimilate the meteorological data into a domain covering the southern half of Brittany and its Atlantic coast (Fig. 1b). Version 3.2 of the WRF model was selected for its state-of-the-art numerical schemes, the apparent ease of use for real-world simulations, the pre-processing packages to assimilate the synoptic meteorological data, and the availability of a software interface in the ARPS package ensuring compatibility between the WRF-model output data and the ARPS-model input data.

## 2.1 Models

The ARPS model is a non-hydrostatic and compressible model generally used in the large-eddy simulation (LES) mode (Xue et al. 2000, 2001). The latest version available at that time (ARPS version 5.2.9) was used. The equations were solved on horizontally-homogeneous grids (see the parameters in Table 1), which were identically stretched in the vertical, with an average vertical grid spacing of 200 m. Model selections included the fourth-order finite-difference advection scheme for horizontal advection, second-order vertical advection, and

**Table 1** Characteristics of the simulations

Grid name	Domain size (km)	Horizontal cell #	Horizontal grid size (m)	Vertical extension	Vertical cell #	Vertical grid size (m)		Integration timestep (s)	Acoustic timestep (s)	Update interval (h)
						Minimum	Mean			
ARPS-100m	14.6 × 15.3	146 × 153	100	6000 m	30	10	200	0.5	0.2	1
ARPS-300m	32.4 × 24.0	108 × 80	300	6000 m	30	10	200	1	0.5	1
ARPS-1km	105 × 78	105 × 78	1000	6000 m	30	10	200	2	1	1
WRF-5km	250 × 200	50 × 40	5000	100 hPa	41	100	400	10	/	6

the vertically-implicit treatment of the vertical velocity component and pressure equations. The horizontal and vertical computational mixing coefficients (for damping high-frequency fluctuations) were both set to  $10^{-3} \text{ s}^{-1}$  after several tests of numerical stability, while the Coriolis terms are included in the equations for the horizontal velocity components. A zero gradient was applied as the top boundary condition, with a Rayleigh damping layer above 4000 m. At the bottom boundary, the momentum, heat and moisture surface fluxes are computed from Monin-Obukhov similarity-theory using stability-dependent drag coefficients and surface temperature and moisture. For the land surfaces, these variables are computed with the ARPS soil-vegetation model based on [Ek and Mahrt \(1991\)](#) and [Chen and Dudhia \(2001\)](#), as described in Sect. 2.2, whereas constant values are assumed over the sea surface. At the lateral boundaries of the nested domains, a transitional zone of five grid meshes ensured the transition between the external forcing from the larger domain and the inner simulation. A non-local PBL parametrization was selected for the treatment of convective boundary-layer turbulence, with a combination of the three-dimensional, 1.5-order [Deardorff \(1980\)](#) subgrid-scale (SGS) turbulence scheme for the horizontal turbulent mixing and the closure scheme of [Sun and Chang \(1986\)](#) that relates the vertical mixing length to the (non-local) PBL depth ([Xue et al. 2000](#)). This option is discussed further in Sect. 5. The Kessler warm-rain microphysics and the Kain–Fritsch scheme ([Kain and Fritsch 1993](#)) for convective cumulus parametrizations were activated, as well as the simplified surface-radiation-physics option.

The WRF model ([Skamarock et al. 2008](#)) solves the fully-compressible Reynolds-averaged Navier–Stokes equations on a terrain-following grid. The following schemes were selected: the rapid radiative transfer model for longwave radiation ([Mlawer et al. 1997](#)), [Dudhia's \(1989\)](#) scheme for shortwave radiation, the MM5 similarity scheme for the surface-layer fluxes based on standard Monin–Obukhov similarity functions with the Carlson-Boland formulation for the moisture flux ([Carlson and Boland 1978](#)), and the Yonsei University scheme (YSU, [Hong et al. 2006](#)) for the PBL parameterization. The Noah Land-Surface Model was used for the temperature and moisture of the soil and vegetation.

[Hu et al. \(2013\)](#) reported that several studies indicate that the YSU-PBL parametrization implemented in the WRF model prior to version 3.4.1 performed less well at night than during the day due to an error enhancing the eddy viscosity under stable conditions, thereby generating large biases during night-time. [Hu et al. \(2013\)](#) concluded that version 3.4.1 of the model produced better agreement with observations than the previous version. Although their analysis does not allow us to draw any firm conclusion for [Herlédant's \(2011\)](#) simulations with the WRF-model version 3.2, this is the reason why we do not include the night-time and transitional periods in the present reanalysis.

The WRF pre-processor ensured the interpolation of the synoptic meteorological data on the computational grid. The data were provided at  $1^\circ$  resolution every 6 h from the Global Forecast System model analysis of the National Center for Environmental Prediction (NCEP, <http://www.ncep.noaa.gov/index.php?branch=GFS>). In addition, the pre-processor was used to extract the relief and land-cover data corresponding to the computational grid from the National Center for Atmospheric Research (NCAR) database (<ftp://ftp.ucar.edu/mesouser/MM5V2/Terrain/terrain.tar.gz>).

## 2.2 Terrain Parameters

The ARPS model includes a soil model that computes a composite ground-vegetation surface-skin temperature by solving the heat- and water-transfer equations at the surface, through the vegetation and through a number of soil layers. Five soil layers were used, with the upper one of 0.2-m thickness, with the soil model containing 13 soil types (including water and ice)

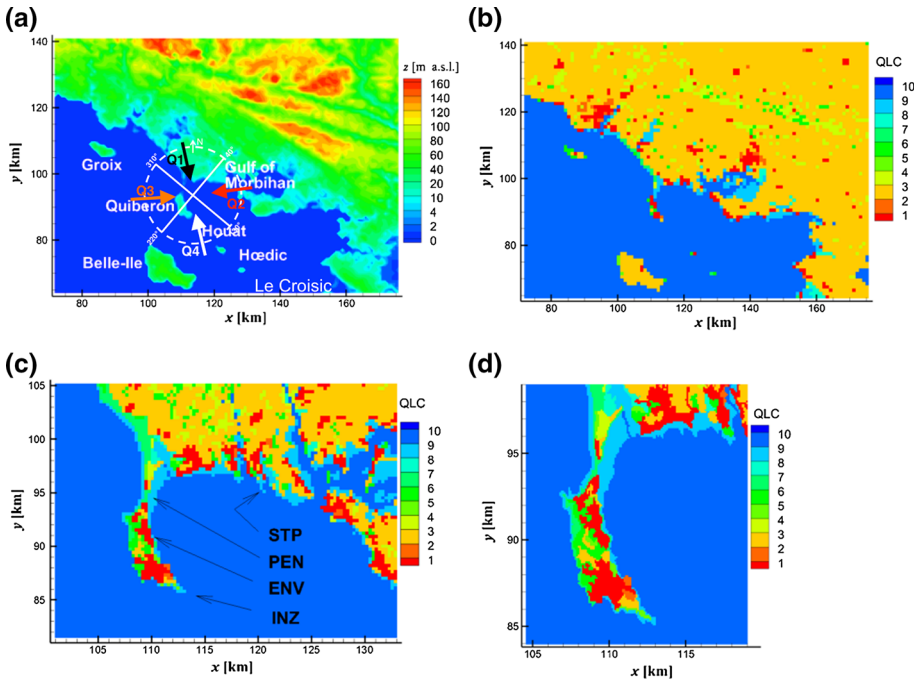


**Fig. 2** The ARPS-model computational domains at the grid spacing of 1 km (a, b), 300 m (c) and 100 m (d). In panel a the colours indicate the height above mean sea level of the 1-km meshes; in panels b, c and d the colours indicate the dominant land-cover mode (QLC class, see Table 2); panel a shows the synoptic wind quadrants and panel c shows the measurement sites at Saint Philibert (STP), Penthièvre isthmus (PEN), the National Sailing School (ENV) and Iniz en Toul Braz islet (INZ). The geographical coordinates of the bay centre are  $47.31^{\circ}\text{N}$ ,  $3.03^{\circ}\text{W}$  and those of the origin (0,0) of the model coordinate system are  $46^{\circ}41'22''\text{N}$ ,  $4^{\circ}33'58''\text{W}$

and 14 vegetation types. The Coordination et Recherche d'Informations sur l'Environnement (CORINE) land-cover database level 3 (CEC 1993) was used to classify the ground-cover modes of the 100-m resolution grid. The CORINE land cover (CLC) level 3 includes 44 cover modes, half of which are present in the computational domains. To adjust the CLC modes to the ARPS soil and vegetation types, [Herlédant \(2011\)](#) merged them into an ad-hoc classification of 10 modes, called Quiberon land-cover (QLC) classes (Table 2), based on similarities and differences in albedo, height/roughness length and soil composition. The proportion of each QLC class in each mesh of the three computational grids was computed with the open-source geographical-information system OrbisGIS ([Bocher and Petit 2012](#)), which allowed selection of the dominant QLC class in each mesh. With this procedure, the surface specification was coherent with the spatial resolution of each computational grid independently of the other grids (Fig. 2). The 100-m grid spacing reveals the full diversity of land-cover modes, the complexity of the shoreline and the large extent of the intertidal mud flat (Fig. 2d).

The topographical data were extracted from the “BD ALTI® 500” database of the French National Geographical Institute and processed with OrbisGIS to interpolate the mean height above mean sea level (a.s.l.) of each grid point in the three grids, with a vertical resolution of less than 1 m (Fig. 2a). Figure 2 shows that the domain of principal interest, the semi-circular bay where the experimental campaign took place, is included in the larger basin of Mor Braz.

**Table 2** Land-cover modes in the Quiberon simulations

QLC <sup>a</sup> mode	QLC class	CLC <sup>b</sup> mode	CLC class	Roughness length (m)	ARPS soil type <sup>c</sup>	ARPS vegetation type <sup>d</sup>
Urban	1	Urban discontinuous	112	1.5	6	5
Industrial area	2	Industry and commerce	121	1	6	3
		Harbour	123			
Rural		Airport	124			
	3	Sport, recreational	142	0.15	6	10
		Agricultural plots	211, 242, 243			
Forest		Prairies	231			
	4	Deciduous	311	0.8	6	6
Pasture		Coniferous	312			
		Mixed	313			
Heath	5	Lawn, pasture	321	0.1	6	3
	6	Heath	322	0.05	9	4
Sand		Bush, shrubs	324			
	7	Beach, dune, sand	331	0.5	1	12
Marsh		Sparse vegetation	333			
	8	Marsh	421, 422	0.01	13	11
Mud flat	9	Intertidal area	423	0.05	1	11
	Sea		Estuary	522	0.0005	13
		Sea, ocean	523			

<sup>a</sup> QLC = Quiberon land cover; <sup>b</sup> CLC = CORINE land cover; <sup>c</sup> ARPS soil types: 1 = sand, 6 = sandy clay loam, 9 = sandy clay, 13 = water; <sup>d</sup> ARPS vegetation types: 3 = grassland with shrub cover, 5 = grassland with tree cover, 6 = deciduous forest, 11 = bog or marsh, 12 = dwarf shrub, 14 = water

The seabed of this basin is separated from the open sea by a line of shallows joining the Quiberon foreland, the Houat and Hœdic islands, up to Le Croisic on the east. The mainland coast is cut by several long river mouths (rias) and the Gulf of Morbihan. In contrast, the coast is rectilinear for about 20 km on the west of the peninsula.

The simulations included the following simplifications of the sea surface: (i) a constant sea level corresponding to the low tide, while considering the intertidal mud flat area as a humid land surface with a roughness length of  $5 \times 10^{-2}$  m; (ii) a constant and homogeneous roughness length of  $5 \times 10^{-4}$  m, corresponding to the roughness length observed at a wind speed of  $2.5\text{--}3 \text{ m s}^{-1}$  (Smith 1988); (iii) a constant and homogeneous surface temperature of  $15.8^\circ\text{C}$ . This last assumption is supported by our sea-surface-temperature monitoring during the campaign, and thus providing a very useful simplification of the model computation (see Sect. 6.4).

### 2.3 Simulation Procedures

The WRF-model simulations were run over 48-h time frames starting at 0000 UTC, with lateral conditions imposed from the NCEP meteorological files every 6 h, the atmospheric initial conditions interpolated from the first NCEP file, and model output data saved every hour. The ARPS model simulations were initiated at the same time as the WRF-model computations. The atmospheric initial conditions of the ARPS-1km domain were interpolated from WRF-model outputs at 0000 UTC: as such, they were a spatial interpolation of the NCEP data and were almost horizontally homogeneous over the whole domain. Similarly, the initial fields of the ARPS-300m and ARPS-100m domains were provided by an interpolation of the ARPS-1km and ARPS-300m fields, respectively. The initial conditions in the soil model were imposed from an analysis of the meteorological conditions of the previous day and on the measurements at the Penthièvre isthmus site (see Part 1).

During the runtime, forcing conditions were imposed at the lateral boundaries of the three nested grids (see Fig. 1a) based on the hourly output data of the coarser grids. A linear interpolation at the intermediate timesteps of the nested grids provided the lateral-boundary forcing between update intervals (Table 1).

In addition to the hourly atmospheric fields, the velocity and temperatures computed with the ARPS model were time-averaged over 15 min using the results of all timesteps (Table 1). At the grid points corresponding to the measurement sites, the mean variables were registered every 15 min for comparison to the experimental data. The available output database includes these 15-min time series and the hourly velocity and temperature fields at the first level of the four computational grids. Since the 5-km grid spacing of the WRF domain does not resolve the peninsula and the bay, a central grid point on land was selected on the northern coast of Quiberon bay as being representative of the mesoscale atmospheric behaviour over this part of the southern Brittany coast.

## 3 Comparison of Simulations with Measurements

Out of the three 48-h time frames simulated by [Herlédant \(2011\)](#), we concentrate here on the two days of 23 and 27 June analyzed in Part 1. On 23 June, the synoptic flow was directed offshore from quadrant 2 (Q2) or quadrant 1 (Q1, see the quadrant limits in Fig. 2a) giving rise to a sea breeze. On 27 June, a weak westerly synoptic wind direction gave rise to a thermal reinforcement or synoptic breeze.

The figures in the remainder of this section depict the measurements obtained at 10 m above ground level (a.g.l.) at the coastal site of Saint Philibert, at 28 m a.g.l. at the Penthièvre

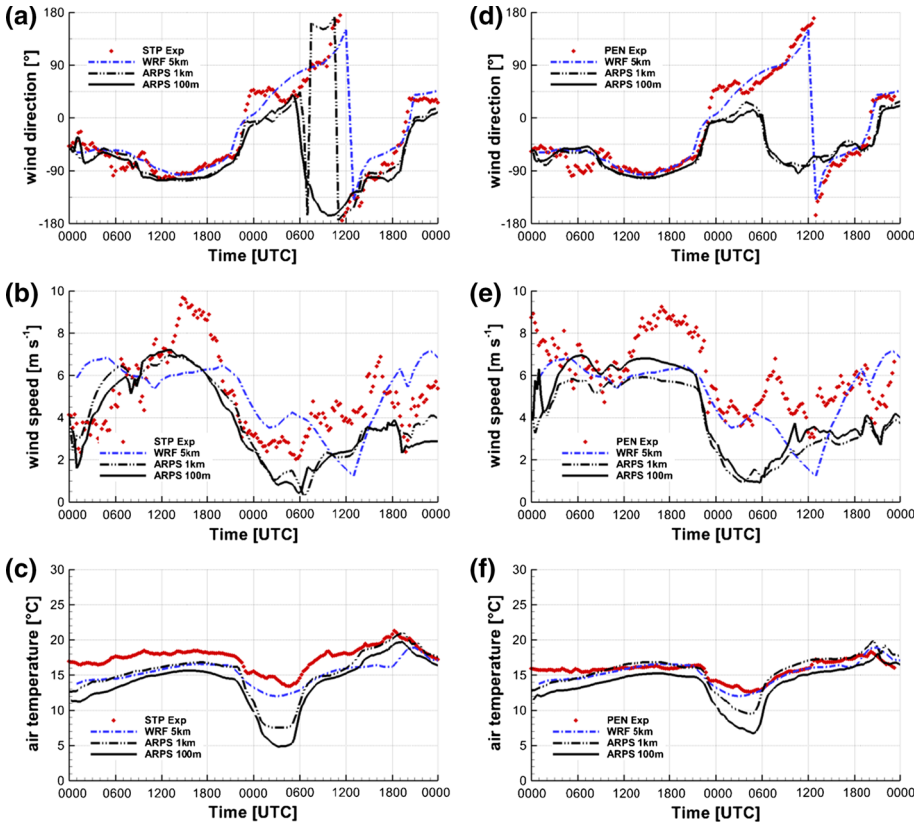


**Fig. 3** Time series of 22–23 June measured (dots) and simulated (lines) wind direction (a, d), wind speed (b, e) and air temperature (c, f) at the Saint Philibert coastal site (a–c) and the Penthièvre isthmus site (d–f); the time axis starts at 0000 UTC on 22 June

isthmus site, and at 8 m a.g.l. at the southern offshore site on the islet of Iniz en Toul Braz (Fig. 2c, INZ, hereafter the Toul Braz islet). The simulation data correspond to the first computational level at 5 m and 50 m a.g.l. for the ARPS and WRF models, respectively. Due to these differences, Figs. 3, 4, 5, 6 and 7 do not represent any sort of model validation, but we prefer comparing these raw measurements and simulation data rather than data interpolated to a common height with a disputable interpolation method. Therefore, the reader must keep in mind the differences in heights and origins of the data and consider overall trends rather than absolute values. Although not directly comparable with the measurements, the WRF data for the central grid point on land are reported in the figures for conciseness. Their presentation is informative because they are representative of the mesoscale velocity field forcing the ARPS model.

### 3.1 Sea Breeze of 23 June

In this section, although our analysis is limited to the daytime period of 23 June, the results of the complete 48-h runs starting at 0000 UTC on 22 June are reported for clarity (Figs. 3, 4, 5).



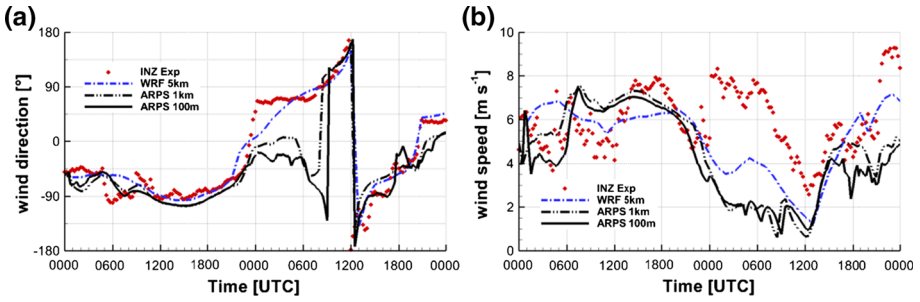


**Fig. 4** Time series of 22–23 June measured (dots) and simulated (lines) wind direction (a) and wind speed (b) at the offshore Toul Braz islet site; the time axis starts at 0000 UTC on 22 June

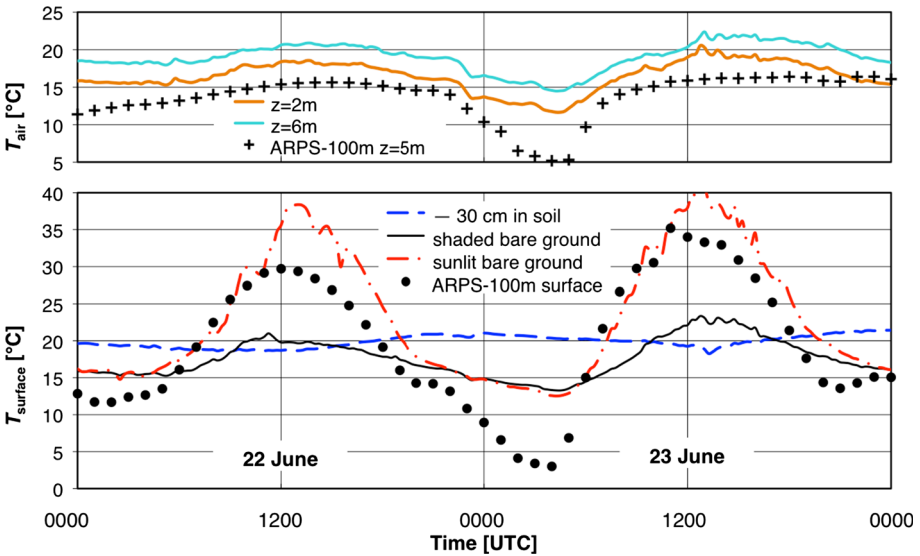


**Fig. 5** Surface and air-temperature measurements at the sunlit and shaded bare-ground surfaces, in the surface soil layer at  $z = -0.3$  m, and at  $z = 2$  m and 6 m a.s.l. (lines), and in the ARPS-100 m simulation (symbols), at the Penthièvre isthmus site on 22–23 June; the time axis starts at 0000 UTC on 22 June

The mesoscale wind direction and the daytime clockwise rotation for these two days are well simulated with the WRF model, except during the early morning of 23 June when the details of the night-to-day transition period are unduly smoothed. As explained above, we do not comment on the WRF model results obtained for the day of 22 June, which are only presented here to show the simulation continuity of the night-time and the transitional period. While wind speeds do not compare well, the overall trends are reproduced. The WRF model data do not reproduce the local variations (that are different at the three sites) for the early morning of 23 June, but the mesoscale breeze onset appears correctly around 1300 UTC, as observed in the detailed analysis of Part 1. The air-temperature comparisons show a persistent underestimation by about 3 °C at the Saint Philibert coastal site, but less at the Penthièvre isthmus site.

Since the ARPS-300m results always sit between those from the ARPS-1km and ARPS-100 m domains, only the time series of these last two simulations are reported to avoid crowded

figures. On 22 June, the wind direction is simulated as well with the ARPS model as with the WRF model, while the ARPS model also reproduces the short-term fluctuations evident in the measurements, albeit not always exactly in phase. The night-time and early-morning simulations on 23 June with the ARPS model show an anti-clockwise rotation (backing), and thus do not reproduce the measurements well, which show a continuous wind veering. We can attribute this to the passage of a front at around 2300 UTC, which does not appear in the NCEP meteorological file of 0000 UTC and, consequently, its impact is not transmitted from the WRF model to the ARPS model before the 0600 UTC update. The ARPS-model simulations rejoin the measured wind directions at 0900–1000 UTC at the southern offshore site (Toul Braz islet) where the wind speed is well reproduced in the afternoon, at 1200–1300 UTC at the Saint Philibert mainland coastal site and not before 1500 UTC at the Penthièvre isthmus site, where the afternoon wind speed is somewhat underestimated, perhaps due to a slight temperature underestimation.

The surface temperatures simulated with the ARPS-100m soil model are compared with the measurements at the Penthièvre isthmus site in Fig. 5, despite the different definitions. The measured temperatures were obtained at one point (see Part 1 and the caption of Fig. 5), while the model temperature is the ARPS composite ground–vegetation surface-skin temperature above the sandy soil integrated into the grid cell at the Penthièvre site. Despite these differences and the lack of temperature observations at additional sites, it is clear that the daily variations of the simulations are in reasonable agreement with the measurements during daytime, although it is difficult to be conclusive in view of the very large differences between the sunlit and shaded bare-ground temperatures. However, the night-time model temperatures are significantly lower than the measurements. The cause of the ARPS soil-model failure is not clear since the land-cover modes have been selected with great care (see Sect. 2.2). Probable explanations are an underestimation of the initial soil moisture, which is known to induce soil-model over-reactions (Calmet et al. 2007; Calmet and Mestayer 2016), or the chosen predominance of sand in the soil composition. The low ground temperatures in the simulations explain the underestimated air temperatures at the Saint Philibert mainland coastal site (Fig. 3c). In contrast the measured and modelled air temperatures differ less at the Penthièvre isthmus site (Fig. 3f), because this site is more influenced by the marine air and less by the surface heat flux. However, the simulated wind speeds are lower than those measured, leading to less horizontal advection from sea to land, and, hence, less coupling between the sea and land than actually occurred.

### 3.2 Thermal Reinforcement of 27 June

This day was rather typical of a quadrant-3 flow, with a weak synoptic flow from the west giving rise to the strong daytime thermal reinforcement of the flow; we labelled it as a “synoptic breeze” in Part 1. The model-to-measurement comparison is reported in Figs. 6 and 7, with the model runs starting at 0000 UTC on June 27. The results of these simulations are rather satisfactory. The WRF model data correspond quite well with the average of the measurements at the three sites, which is probably representative of the mesoscale flow, although there is often a clear 1–2 h time lag. The wind speeds are slightly underestimated during the breeze periods of the afternoon, and slightly overestimated in the evening, probably due to the lower model temperatures over the land surfaces. As expected, because the WRF model data are representative of the bay area, the agreement is even better with the measurements at the Toul Braz islet offshore site (Fig. 7).

The ARPS-model local simulations generally show a better agreement with the local measurements than the WRF model simulations, with notably less time lags, demonstrating

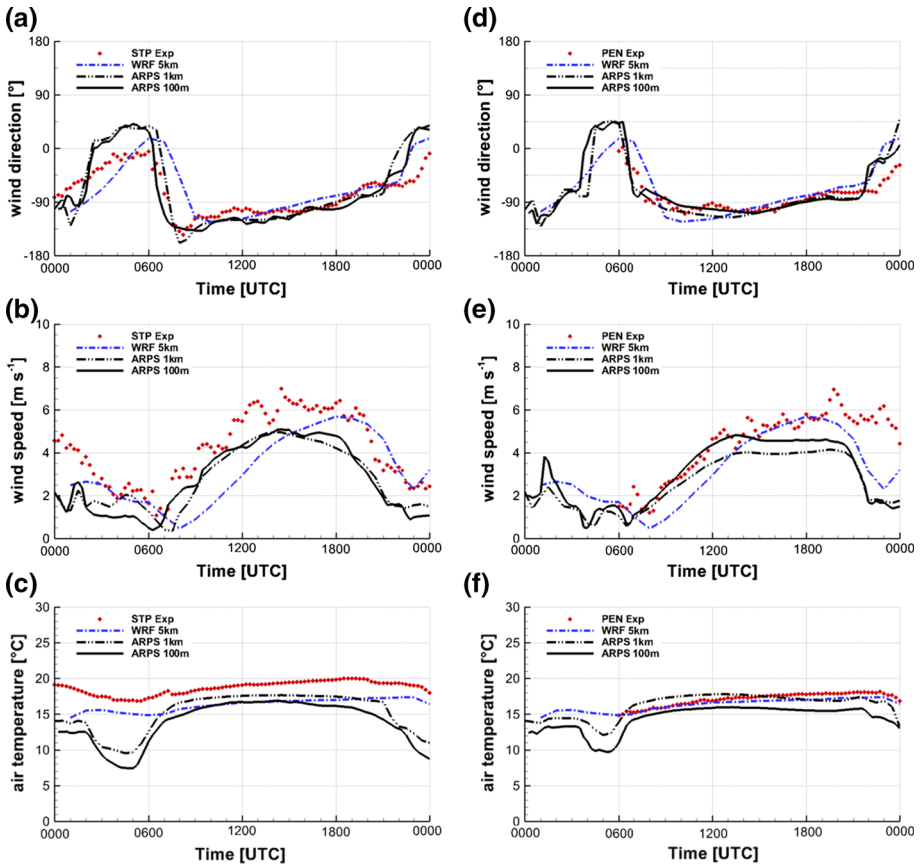


Fig. 6 Time series of 27 June, as for Fig. 3, but the time axis starts at 0000 UTC on 27 June

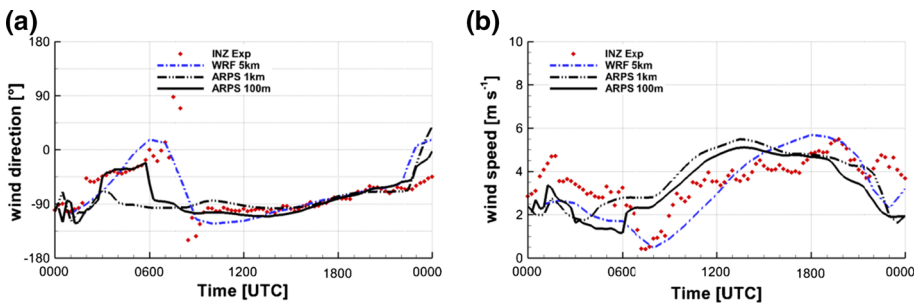


Fig. 7 Time series of 27 June, as for Fig. 4 but the time axis starts at 0000 UTC on 27 June

that the local coastal influence is not negligible and rather well reproduced with the high resolution simulation. The wind speeds seem moderately underestimated, but this is due to the difference in heights (5 m in the ARPS model, 16 m at the Penthièvre site, 10 m at the Saint Philibert site and 8 m at the Toul Braz islet site), with any variation still in phase with the measurements. At the mainland and isthmus sites, Penthièvre and Saint Philibert, the

anti-clockwise rotation of the wind direction during the early-morning transitional phase of 27 June is well simulated; at the southern offshore site, the strong variations of the wind direction are clipped.

After this early morning transitional phase, the ARPS-model simulations reproduce well the observed wind directions. The simulations for the three sites corroborate the analysis of the experimental data presented in Part 1: an early breeze onset at 0600 UTC at the mainland site, followed by a later breeze onset at the isthmus and southern sites after 0900 UTC, which is in agreement with the breeze-front propagation above the peninsula towards the bay.

## 4 Wind Fields Simulated with the ARPS Model During Daytime

We present here horizontal cross-sections of the velocity field obtained with the ARPS model at the first computational vertical level located 5 m above the surface. To ensure legibility, we show only one out of three or five simulated wind directions, but all wind-speed isocontours were computed with the full numerical resolution. The black lines in these figures correspond to the low-tide level, including the smooth mud flats within the land surfaces.

### 4.1 Sea-Breeze Onset and Development on 23 June

In the early morning, the synoptic flow was directed from the north-east, implying a quadrant-2 situation. Since the simulations do not reproduce the early-morning transition very well, we begin our analysis at 1000 UTC when the simulations again correspond well to the measurements. At that time, the mesoscale flow had already started a clockwise rotation towards a direction roughly perpendicular to the orientation of the mesoscale coast a few hours before. The mesoscale breeze is already well-structured along the rectilinear coast to the west of the peninsula (Fig. 8), while to the east, due to the complicated shape of the coastline, the breeze has yet to develop, with a large zone of stagnant flow occupying the centre of the basin, and flow acceleration towards the local coasts. Over the mainland, the

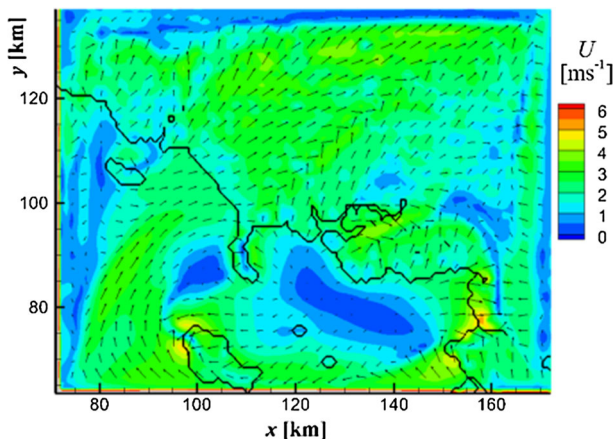


**Fig. 8** Cross-section of the velocity field at the 5-m level above the surface during the sea-breeze development on 23 June at 1000 UTC within the ARPS-1km domain, with the colours representing the wind speed (one vector out of three is shown)

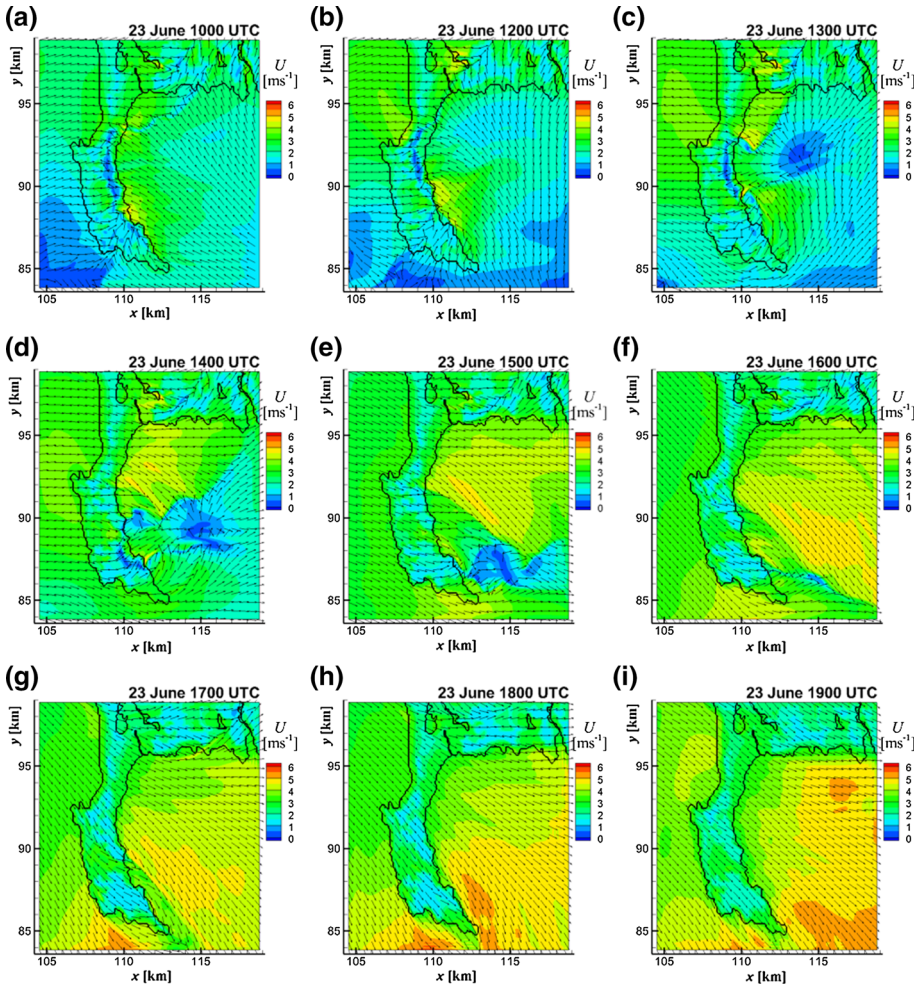


**Fig. 9** Cross-sections of the velocity field at the 5-m level above the surface during the sea-breeze development on 23 June within the ARPS-100m domain, with the arrows indicating the wind direction and the colours representing the wind speed (one arrow out of five is shown)

convergence of the two mesoscale breeze branches from the west and east gives rise to an inner front. The flow enters the Quiberon bay from the south-east (see Figs. 8 and 9a).

Initially (1000–1200 UTC), the flow arriving at the coast is directed approximately perpendicular to the local coastal orientation at a 1-km scale (Fig. 9a, b). The south-westerly mesoscale breeze generated by the coastal orientation may be seen along the western border of the smaller domain. The wind-speed differences on the two sides of the peninsula generate an arched local breeze front along the eastern coast and over Quiberon itself (i.e., the southern part of the peninsula, south of Penthièvre isthmus), with the first acceleration in the area of the bay site (National Sailing School, ENV, see Fig. 2c). In the northern part of the bay, the sea breeze accelerates between two zones of stagnant flow: the first zone is above the coastline, while the second zone appears as a large round patch 2–3 km in diameter, and centred about 3–4 km from the shore. We consider this circular zone of stagnant flow to be the counterpart



for the semi-circular bay of the offshore band of calms described by [Houghton and Campbell \(2005\)](#) for a linear coast in a quadrant-2 condition (see Sect. 2.2 of Part 1).

All around the bay, local breezes accelerate as the ground temperatures increase. At 1300 UTC, the bay is fed by a westerly breeze circling the south of the peninsula and the Quiberon foreland. The offshore zone of stagnant flow moves further offshore, yielding to the development of the sea breeze in the northern part of the bay, and over the mainland. Over the land, the flow-convergence front is clearly visible. In the north-west corner of the bay, the westerly flow over the flat strip of land induces the onset of a local “land breeze” thrusting the breeze front 1.5 km offshore (Fig. 9c).

After 1300 UTC, as the mesoscale breeze is reinforced, and progressively veers in the north-westerly sector, this zone of greater wind speeds invades the bay, close to the coast at first (Fig. 9c, d), then over the complete bay area (Fig. 9e, f), while displacing the offshore zone of stagnant flow further southwards. Thus, the front between this strong north-westerly flow and the remains of the local sea breeze moves southwards in the southern part of the bay and eastwards in its northern part. This explains our measurements on the catamarans along the west-north-west to east-south-east transect from the isthmus (Penthievre site) through the bay centre (compare Fig. 7 of Part 1): the wind-fanning effect downwind from the isthmus, which is typical of the Quiberon bay, is especially visible in the wind directions shifting from the west in the north of the bay, to the north-west in the south. The flow circling the south of the peninsula weakens, while the zone of stagnant flow moves southwards (Fig. 9d, e) and vanishes (Fig. 9f).

After 1700 UTC, the wind fanning lessens and the velocity field tends to become homogeneous in the dominant north-west direction (Fig. 9g–i). Around Quiberon itself, the zone of encircling flow is replaced by bands of reduced wind speed along the two coasts and a convergence zone in the lee of the foreland (Fig. 9g, h). In the evening, the wind speed remains low in the proximity of the coast, but rapidly increases offshore as soon as the thermal convection yields to a weak stable stratification (see  $z/L_{MO}$  in Fig. 3 of Part 1, and compare with Fig. 6b of Part 1).

To conclude this section, let us note that, according to these simulations, the zone of onshore flow extended over the entire bay in the late morning, whereas, after the breeze onset, the sea-breeze zone covered only the northern half of the bay; this breeze zone shrank in the early afternoon to a narrow band traversing the bay along a south-west to north-east transect and vanished in mid-afternoon.

## 4.2 Thermal Reinforcement or Synoptic Breeze on 27 June

The day of 27 June was a rather typical summer day with a weak south-westerly synoptic flow, strong insolation, and rather strong convection, which is typical of the quadrant-3 regime. Since the night-time evolution and the transition in the early morning are well reproduced by the simulations, we may commence our velocity field analysis as early as 0500 UTC to follow the transition from land breeze to sea breeze and the thermal reinforcement. At that early time, the land breeze is still noticeable in a band along the shore about 10 km in width on the west of the peninsula and only 3–5 km in width over the eastern basin (Fig. 10a), with a breeze front identified by bands of stagnant flow. At 0600 UTC (Fig. 10b), the breeze already vanishes over the land and the synoptic flow from the west to west-south-west is established over the open sea. At 0700 UTC, the zones of stagnant flow have spread over the water along the shores (Fig. 10c), and moved offshore by 0800 UTC, having been replaced by a narrow band of inshore flow spread already over the coast (Fig. 10d).

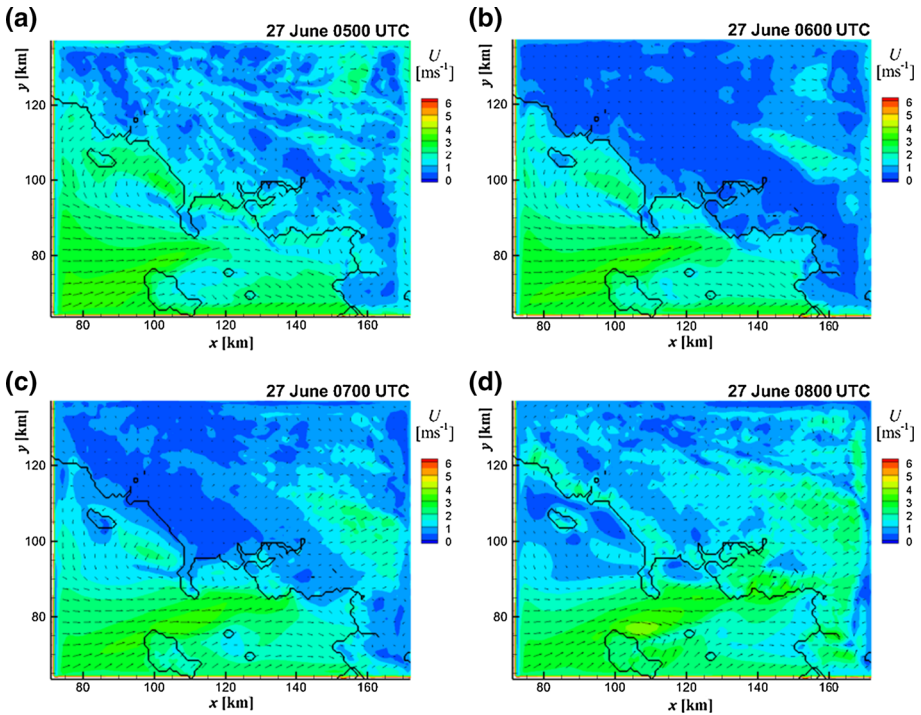


**Fig. 10** Cross-sections of the velocity field at the 5-m level above the surface during the transition phase in the early morning of 27 June within the ARPS-1km domain, as for Fig. 8

Focusing on the bay area (Fig. 11), the land breeze is clearly visible along the shore prior to 0700 UTC (Fig. 11a, b), while the southern part of the domain is occupied by calm zones. An initial front appears at the northern edge of the stagnant zone in the bay, and is slightly reinforced at 0600 UTC while already moving southwards (Fig. 11b). At 0700 UTC (Fig. 11c), we see two bands of stagnant flow parallel to the northern coast of the bay, the first one inshore, and the second one offshore, giving rise to a restricted sea breeze about 1 km in width just over the shoreline.

By 0800 UTC (Fig. 11d), the offshore zone of calms has moved southwards and, merging with the stagnant zone present earlier in the south of the bay, combines to form an enlarged circular region of stagnant flow with a circular breeze front, while the backward rotation of the wind direction continues everywhere else. The position of the calm zone explains why the wind direction observed at the bay centre (see point-R data in Fig. 9 of Part I) was temporarily more northerly than at the other sites. By 0900 UTC, this calm zone has nearly vanished, with its only trace being two weak south-west to north-east fronts (Fig. 11e). Figure 11e also shows the first indication of a flow acceleration along the south-east coast of Quiberon. The thermal reinforcement is seen to develop earlier and with a larger intensity within the bay than on the west of the peninsula, and closer to the eastern coast of the peninsula than over the bay (Fig. 11f, g). The offshore velocity field in the western part of the bay clearly reveals the small-scale wakes generated by the land relief, and the alternation of rocky and sandy shores. In the afternoon, the thermal reinforcement grows stronger over the bay than in the lee of the peninsula where it is decelerated by the stronger friction (Fig. 11h), and already weakens at 1600 UTC (Fig. 11i).



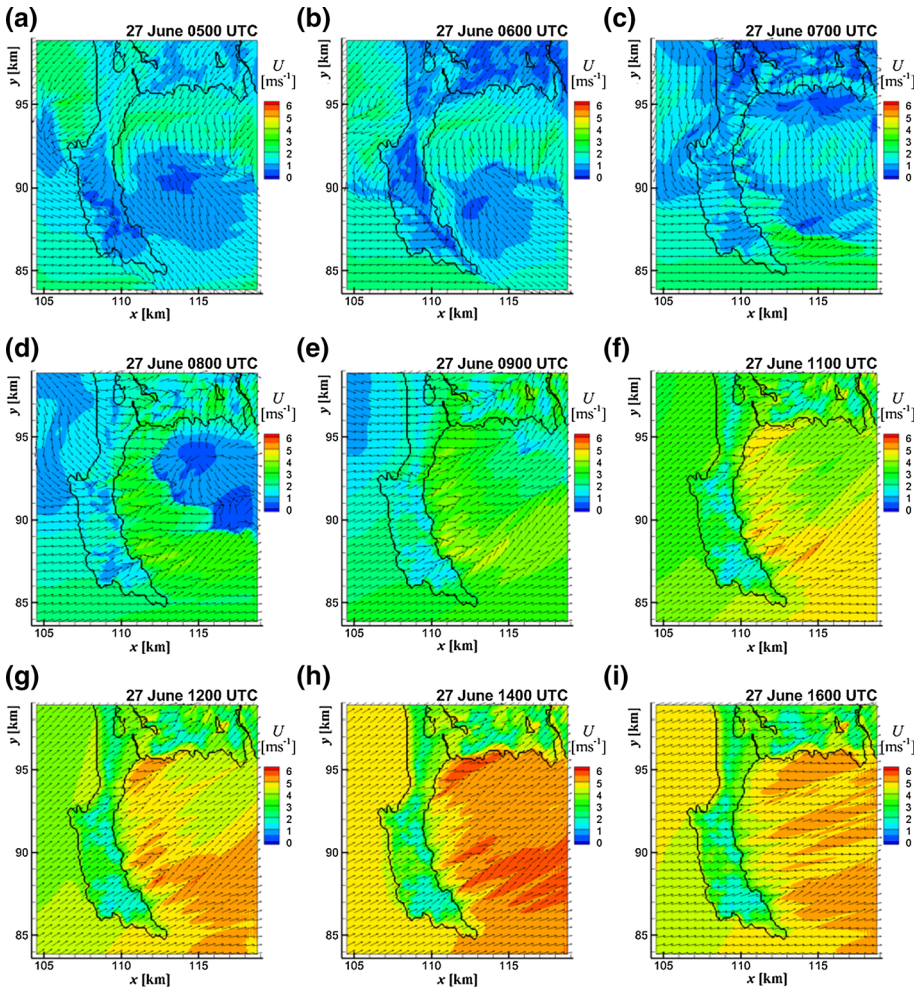


**Fig. 11** Cross-sections of the velocity field at the 5-m level above the surface during the synoptic breeze onset and development on 27 June, as for Fig. 9

### 4.3 Magnification of the Small-Scale Influences of the Quiberon Foreland

The small size of the printed figures oblige us to downscale their apparent resolution (one of three or five vectors displayed) to ensure legibility when presenting the full ARPS-100m domain. Magnification to full resolution at the higher spatial resolution of the model significantly improves visualization of the small-scale processes, especially the local coastal influences close to the shore, but extending sometimes several kilometres offshore. This may not be immediately evident in the comparison with the experimental data because point-to-point and time-to-time comparisons between measurements and numerical simulations are challenging in the absence of a spatial-averaging procedure for the numerical results. Moreover, this difficulty increases with a finer spatial resolution, because the measurements may be better representative of the results of an adjacent computational cell.

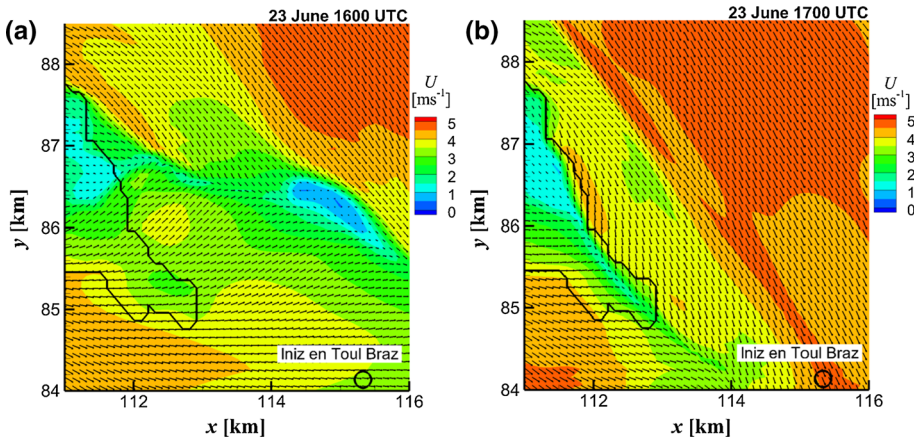


**Fig. 12** Cross-sections of the velocity field at the full 100-m grid spacing for the Quiberon foreland and Iniz en Toul Braz islet on 23 June at 1600 UTC (a) and 1700 UTC (b), with the colours representing the wind speed

Figure 12 presents the magnified area of Quiberon foreland and Iniz en Toul Braz islet during the rapid change of flow pattern between 1600 UTC and 1700 UTC on 23 June. Since the analysis of this episode has been presented in Sect. 4.1, it is not repeated here, but these figures at full resolution, where the arrows represent the horizontal wind vectors, demonstrate the wealth of details provided by ARPS-100m simulations. For instance, we can better quantify the influence of the flow circling around Quiberon in the velocity field in the first kilometres offshore at 1600 UTC, or identify the front at the convergence of the two flow branches arriving from both sides of the peninsula in the lee of the foreland at 1700 UTC, which induces a directional shift of  $15\text{--}20^\circ$  and a deceleration by approximately 25%. The figures also explain the rapid change of wind direction from  $270^\circ$  to  $345^\circ$  observed at the Toul Braz islet site both in the measurements and in the simulations (Fig. 4a).

## 5 Discussion of the Numerical Simulation Strategy

To successfully model breezes over a semi-circular coastal bay, both a large simulation domain and a fine spatial resolution are needed, for which the strategy of [Herlédant \(2011\)](#) was satisfactory. The one-way nesting strategy of the three ARPS domains was also satisfactory, with the smaller domains reacting well to the lateral forcing of the next larger domain, while improving the description of the local-scale influence of the coastal orientation and proximity. The strategy succeeded in addressing our primary objectives of exploring the onset and development of the sea breeze, and the possible small-scale influences of the complex coastal shape on the velocity field during the daytime breeze episodes (i.e. in convective conditions).

Our comparisons of the velocity fields obtained with the grid spacing of 100 and 300 m (not shown) allow us to conclude that, while the 100-m grid spacing only marginally improves the detection of these small-scale influences, it does provide more detailed insight into the flow in sensitive areas, with differences mainly appearing very close to the land–sea transition and in the flow-convergence regions (see Fig. 12). Since the same dataset was used to define the topography of both computational grids, the differences between the results at 100- and

300-m resolutions mainly result from the numerical smoothing of the horizontal gradients, which leaves the question still unanswered as to what extent the simulation of the dynamics of the flow is improved by the very fine spatial resolution. [Michioka and Chow \(2008\)](#) stated that, while the finer resolution improves the computation of turbulence parameters, only little improvement in the mean wind speed and direction is attained. While the 300-m grid spacing may be sufficient for simulating most details of the velocity field, the 100-m grid spacing should improve the simulation of those turbulence parameters necessary for the study of, e.g., electromagnetic propagation or wind-gust statistics.

The thorough comparisons of simulation results with the Quiberon 2006 measurements (Sect. 3) reveal three weak points of the modelling strategy: the low resolution of the WRF model simulation, the weak forcing of the largest LES domain by the WRF model simulation, and the surface temperature underestimation of the ARPS soil model (principally at night).

The WRF code (model and pre-processor) used to assimilate the meteorological data from the Global Forecast System simulated the mesoscale wind directions well, although the 5-km horizontal grid size did not reveal the influence of the main islands or the peninsula separation between the Mor Braz basin to the east and the more open marine zone to the west. Furthermore, the vertical resolution of the WRF model simulation was too low, with the 100-m thickness of the first grid layer preventing the accurate simulation of the surface wind speeds.

The conditioning of the largest ARPS domain by the WRF model simulation for assimilation of the meteorological data was not optimal. The forcing at the lateral borders of the 1-km domain was too weak and did not reproduce well the balance between the mesoscale and local-scale influences in the velocity field. Therefore, the necessary improvements are presented in Sect. 6.4.

As the temperature of the land surfaces is known to be a critical modelling point in the simulation of breeze systems, the land-cover characteristics were considered here with great care. However, the soil model may have nonetheless been one cause of the deficiencies in the night-time velocity-field evolution due to inaccurate soil composition, upper soil-layer depth or soil-humidity initialization.

As for the turbulence model, the choice of the non-local formulation of [Sun and Chang \(1986\)](#), which is primarily designed for a Reynolds-averaged approach to turbulence parametrization, may be disputable. In the 1.5-order turbulent kinetic energy (TKE) closure scheme ([Xue et al. 2000](#)) for estimating the velocity scale required in the SGS flux modelling, the mixing lengths are different in the vertical and horizontal directions because of the anisotropy of the turbulence. In Sun and Chang's (1986) formulation, the length scale used for modelling the SGS stress-tensor components  $\tau_{11}$  and  $\tau_{12}$  is the horizontal grid spacing, following Deardorff's (1980) original scheme, whereas a vertical length scale based on the height above ground and the PBL depth is used in the dissipation term of the TKE equation and in the turbulent mixing coefficient for the  $\tau_{13}$  component. The consequence of this combined approach could be an increase of the vertical turbulent mixing in convective situations (compared with the use of the vertical grid spacing of the original scheme), while the mesh influence on the horizontal mixing is preserved. This option, which was chosen in view of the successful simulation of the vertical structure of the breeze cell, may have been a model weakness for the night-time episodes, although under stable conditions or above the convective boundary layer the length scale is supposed to revert back to the Deardorff scheme ([Xue et al. 2000](#)). Close to the surface, as the two schemes yield length scales of approximately the same magnitude, this option had little impact on the results presented here. However, sensitivity analyses would be necessary to clarify this point.

## 6 Conclusion

The analysis of the simulated velocity and temperature fields at the surface leads us to several conclusions about the breeze in coastal regions that were not so obvious from the measurements at the various sites close to the shores. Successes and failures in the simulations also reveal some provisional conclusions about the simulation strategy and possible improvements.

### 6.1 Concerning the Breeze Regimes

The quadrant classification is once more demonstrated to be a powerful method for the prediction of the general behaviour of the breeze during the day. But it must be applied at the mesoscale and with discernment. The mesoscale surface wind speed is not necessarily the average of the local surface observations, especially when observations from the open sea are unavailable. Instead, the synoptic wind direction should be deduced from the regional pressure charts and vertical soundings. Where the coastal orientation is variable, our observations of the early-morning velocity fields (not shown) suggest that the breeze regime depends on the upwind flow: the relevant synoptic wind direction is that observed just after sunrise or expected in the early morning, and the relevant coastal orientation is that of the area upwind from the zone of interest (e.g., for a westerly flow, the wind direction must be compared to the mesoscale coastal orientation to the west of the site of interest). The breeze regime, especially its establishment phase, depends not only on the situation just after sunrise, but also on the recent meteorological and micrometeorological history, especially the wind direction during the preceding night (land breeze or not, synoptic variations, etc.) as summarized in Fig. 11 of Part 1.

### 6.2 Concerning the Breeze Surface Structure

The breeze patterns are much more complex in a semi-circular coastal bay than those reported in the literature for a rectilinear or slightly curved coast. The bands of calms become rounded, the fronts bend, and inner fronts appear after convergence of the different local flows. The velocity field is a complex, non-linear combination, and not just a superposition, of mesoscale and local-scale influences, which are numerous. Instead of the rather continuous process described in text books, the breeze patterns over the bay change quite rapidly under these various influences, and are sometimes spatially and temporally contradictory, while acting in unison at other times. As a consequence, local measurements at the shorelines are insufficient to depict the changing velocity field over the bulk of the bay.

The 100-m grid size of the finest domain of the ARPS model offers a wealth of details required by sailors to analyze the flow patterns over the bay and close to the shores, as well as any changes during competition.

### 6.3 Concerning the Local Coastal Influences

The simulations clearly demonstrate that the velocity field directly above the water surface is sensitive to the local effects resulting from the small-scale coastal features, including the flow deceleration and thermal reinforcement; flow divergence, partly circling the peninsula and partly passing over it; wakes either limited to a narrow band close to the shore or extending several kilometres offshore. These processes result from the combination of land–sea differences in the topography, surface roughness, surface temperature, and thermal stability

in the atmospheric surface layer, on the one hand, and land relief, the approaching wind direction and the return flow aloft on the other hand: general rules-of-thumb are insufficient for the prediction of their combination. Due to the strong non-linearity of the interaction of small- and large-scale processes, high-resolution simulations appear to be the best tool for forecasting or nowcasting the spatial distribution and amplitude of the local flow variations and the rapid evolution of the velocity field over the bay.

Although the velocity fields presented here give some clues, further understanding of the involved processes could also be obtained by sensitivity studies using perturbed surface conditions in terms of the coastline shape, which may be the most efficient way to determine the extent to which the bay configuration affects the local sea breeze.

## 6.4 Concerning Future Numerical Simulations

While [Herlédant \(2011\)](#) used version 3.2 of the WRF model, the current version of the code is version 3.7.1, which features numerous software improvements, notably to the YSU scheme. The current version of the ARPS model, ARPS 5.3.4, also includes several marginal improvements compared with version 5.2.9. Therefore, we expect to obtain improved simulations using the most recent versions of the ARPS and WRF models.

In further studies, to ensure the best spatial resolution provided by the LES fine computational grid, we would prefer the standard SGS scheme of [Deardorff \(1980\)](#) rather than the mixed scheme using the non-local model of [Sun and Chang \(1986\)](#). A dynamic SGS model, such as the locally-averaged scale-dependent dynamic SGS model developed by [Basu and Porté-Agel \(2006\)](#) and [Basu et al. \(2006\)](#), could be even more suitable for simulating the near-surface fields during complete diurnal cycles, because the common SGS models require substantial grid refinement for the stable stratification found at night ([Basu et al. 2008](#)).

As for the land–surface temperatures, we suggest four improvements: (i) a better adaptation of the ARPS and WRF soil models to the actual soil composition and vegetation; (ii) a more accurate initialization of soil humidity using a longer soil-model “spin-up” time; (iii) an improved assimilation of the meteorological-scale air temperature; (iv) a thinner upper-soil layer (0.1 m). While a sensitivity analysis is needed to test these assumptions, we can state with certainty that the implementation of a high-resolution modelling approach to forecast the breeze behaviour at a competition site, such as the Quiberon bay, requires a careful preliminary validation of the simulated surface temperatures against experimental data, e.g., such as those obtained from thermal infrared satellite imagery.

To improve the meteorological data assimilation and forcing of the ARPS model by the WRF model, we see four possible improvements: (i) A finer vertical resolution in the WRF domain, and an additional intermediate-size WRF domain would assimilate the meteorological data, while taking into account the variety of coastal orientations and ground-cover modes at an improved accuracy. (ii) The one-way off-line nesting procedure could be largely improved by an increased update frequency of the forcing by the next largest domain ([Michioka and Chow 2008](#)). Events such as the passage of a front or a rapid shift of the wind direction, as observed around 2300 UTC during the night of 22–23 June, cannot be correctly simulated without the assimilation of meteorological observations at a higher frequency. (iii) A nudging procedure inside the nested domains may improve the transmission of the meteorological forcing into the higher-resolution domains, but it should be restrained to the relatively homogeneous areas far from the coasts and the bay. (iv) The lateral forcing could also be reinforced by a stronger weighting coefficient in the band of influence (transitional zone). Here again, solely sensitivity studies can provide the right answers.



Finally, let us note that, although supported by our measurements, our simplified representation of the sea surface neglects the dynamics of the ocean and bay waters, and the reaction of the surface to the flow variations, which could become more important in other circumstances. There is a large potential for improvements, especially for sailing competitions, by taking into account the surface-roughness variations as a function of the sea state, wind speed and direction. The tidal variations and the associated currents may also be of importance, as well as the variations of sea-surface temperature, but these improvements would require the implementation of significantly more complex simulation strategies.

We hope that this reanalysis helps motivate the initiation of new studies of coastal meteorology with powerful state-of-the-art numerical models.

**Acknowledgements** The authors acknowledge the funding of O. Herlédant's doctoral work by the Centre National de la Recherche Scientifique (CNRS) and the Région des Pays de la Loire. This work was granted access to the HPC resources of CINES (Centre Informatique National de l'Enseignement Supérieur) under the allocation 2009015103 made by Grand Equipement National de Calcul Intensif (GENCI). We also acknowledge the numerous positive recommendations of an unknown reviewer. The background of Fig. 1b is a map from Géoportail. Trade names and companies are given for the benefit of the reader and do not imply any endorsement of the product or company by the authors.

## References

- Adams E (1997) Four ways to win the sea breeze game. *Sailing World* (March):44–49
- Antonelli M, Rotunno R (2007) Large-eddy simulation of the onset of the sea breeze. *J Atmos Sci* 64:4445–4457. <https://doi.org/10.1175/2007JAS2261.1>
- Barré S, Calmet I, Herlédant O, Hiachkine P, Kobus JM, Mestayer PG, De Nomazy C, Piquet T, Quillard O, Rosant JM (2007) The Quiberon 2006 experiment: description and first results on the sea-breeze local behavior. In: Preprints, 7th conference on coastal atmospheric and oceanic prediction and processes, San Diego, 10–13 Sept. 2007, Am Meteorol Soc, P 15.1, p 5
- Basu S, Porté-Agel F (2006) Large-eddy simulation of stably stratified atmospheric boundary layer turbulence: a scale dependent dynamic modeling approach. *J Atmos Sci* 63:2074–2091
- Basu S, Foufoula-Georgiou E, Vinuesa J-F, Pahlow M (2006) Revisiting the local scaling hypothesis in stably stratified atmospheric boundary-layer turbulence: an integration of field and laboratory measurements with large-eddy simulations. *Boundary-Layer Meteorol* 119:473–500
- Basu S, Vinuesa J-F, Swift A (2008) Dynamic LES modeling of a diurnal cycle. *J Appl Meteorol Climatol* 47:1156–1174
- Bernot JY (2007) *Météo locale : croisière et régates (in French)*, Gallimard/FFV (Fédération française de voile). Paris, France (ISBN : 978-2-7424-1944-9)
- Bocher E, Petit G (2012) OrbisGIS: geographical information system designed by and for research. In: Bucher B and Le Ber F (eds). *Innovative software development in GIS, ISTE and Wiley*. Geographical Information System series, Uppal pp 25–66
- Calmet I, Mestayer PG (2016) Study of the thermal internal boundary layer during sea-breeze events in the complex coastal area of Marseille. *Theor Appl Climatol* 123:801–826. <https://doi.org/10.1007/s00704-015-1394-1>
- Calmet I, Leroyer S, Mestayer PG (2007) High-resolution simulations of the urban atmosphere in sea-breeze conditions. In: Preprints 7th symposium urban environment. San Diego, 10–13 (Sept. 2007) Am Meteorol Soc Com J6.3
- Carlson TN, Boland FE (1978) Analysis of urban-rural canopy using a surface heat flux/temperature model. *J Appl Meteorol* 17:998–1013
- CEC (1993) CORINE land cover technical guide. Technical Report EUR 1285 EN, Office for the Official Publications of the European Communities, Luxembourg
- Chen F, Dudhia J (2001) Coupling an advanced land surface-hydrology model with the Penn State-NCAR MM5 modeling system. Part 1: model implementation and sensitivity. *Mon Weather Rev* 129:569–585
- Chow FK, Weigel AP, Street RL, Rotach MW, Xue M (2006) High-Resolution Large-Eddy simulations of flow in a steep alpine valley. Part I: methodology, verification, and sensitivity experiments. *J Appl Meteorol Climatol* 45:64–86

- Crosman ET, Horel JD (2010) Sea and lake breezes: a review of numerical studies. *Boundary-Layer Meteorol* 137:1–29
- Deardorff JW (1980) Stratocumulus-capped mixed layers derived from a three-dimensional model. *Boundary-Layer Meteorol* 18:495–527
- Dudhia J (1989) Numerical study of convection observed during the winter monsoon experiment using a mesoscale two-dimensional model. *J Atmos Sci* 46:3077–3107. <https://doi.org/10.1175/1520-0469>
- Ek M, Mahrt L (1991) OSU 1-D PBL Model User's Guide. Department of Atmospheric Sciences, Oregon State University, Corvallis
- Herlédant O (2011) Étude numérique et expérimentale de la micro-météorologie des sites de régates côtières appliquée à la baie de Quiberon. Doctoral Thesis (**in French**), Ecole Centrale de Nantes, pp 218. <https://tel.archives-ouvertes.fr/LHEEA/tel-00980030v1>
- Hong SY, Noh Y, Dudhia J (2006) A new vertical diffusion package with an explicit treatment of entrainment processes. *Mon Wea Rev* 134:2318–2341. <https://doi.org/10.1175/MWR3199.1>
- Houghton D, Campbell F (2005) *Wind strategy*, 3rd edn. Wiley, London, p 128
- Hu XM, Klein PM, Xue M (2013) Evaluation of the updated YSU planetary boundary layer scheme within WRF for wind resource and air quality assessments. *J Geophys Res Atmos* 118:10490–10505. <https://doi.org/10.1002/jgrd.50823>
- Kain JS, Fritsch JM (1993) Convective parameterization for mesoscale models: the Kain-Fritsch Scheme. In: *The representation of cumulus convection in numerical models*. Meteorological Monographs, vol 24. American Meteorological Society, Boston, pp 165–170
- Leroyer S, Calmet I, Mestayer P (2010) Urban boundary layer simulations of sea-breeze over Marseille during the ESCOMPTE experiment. *Int J Environ Pollut* 40:109–122. <https://doi.org/10.1504/IJEP.2010.030887>
- Mestayer PG, Calmet I, Herlédant O, Barré S, Piquet T, Rosant JM (2018) A coastal bay summer breeze study, part 1: results of the Quiberon 2006 experimental campaign. *Boundary-Layer Meteorol* (**this issue**) <https://doi.org/10.1007/s10546-017-0-314-6>
- Michioka T, Chow FK (2008) High-resolution large-eddy simulations of scalar transport in atmospheric boundary layer flow over complex terrain. *J Appl Meteorol Climatol* 47:3150–3169. <https://doi.org/10.1175/2008JAMC1941.1>
- Miller STK, Keim BD, Talbot RW, Mao H (2003) Sea-breeze: structure, forecasting and impacts. *Rev Geophys* 41:1-1–1-31. <https://doi.org/10.1029/2003RG000124>
- Mlawer EJ, Taubman SJ, Brown PD, Iacono MJ, Clough SA (1997) Radiative transfer for inhomogeneous atmospheres: RRTM, a validated correlated-k model for the longwave. *J Geophys Res Atmos* 102:16663–16682. <https://doi.org/10.1029/97JD00237>
- Skamarock WC, Klemp J, Dudhia J, Gill D, Barker D, Duda M, Huang X, Wang W, Powers J (2008) A description of the advanced research WRF version 3. NCAR Tech Note NCAR/TN-475+STR, pp 113
- Smith SD (1988) Coefficients for sea surface wind stress, heat flux, and wind profiles as a function of wind speed and temperature. *J Geophys Res* 93:15467–15472
- Steele CJ, Dorling SR, von Glasow R, Bacon J (2013) Idealized WRF model sensitivity simulations of sea breeze types and their effects on offshore windfields. *Atmos Chem Phys* 13:443–461
- Sun WY, Chang CZ (1986) Diffusion model for a convective layer. Part I: Numerical simulation of convective boundary layer. *J Appl Meteorol Climatol* 25:1445–1453. <https://doi.org/10.1175/1520-0450>
- Xue M, Droegemeier KK, Wong V (2000) The advanced regional prediction system (ARPS)—s multi-scale nonhydrostatic atmospheric simulation and prediction tool. Part I: model dynamics and verification. *Meteorol Atmos Phys* 5:161–193. <https://doi.org/10.1007/s007030070003>
- Xue M, Droegemeier KK, Wong V, Shapiro A, Brewster K, Carr F, Weber D, Liu X, Wang D (2001) The Advanced regional prediction system (ARPS)—a multi-scale nonhydrostatic atmospheric simulation and prediction tool. Part II: model physics and applications. *Meteorol Atmos Phys* 76:143–166. <https://doi.org/10.1007/s007030170027>